Chinese Journal of Chemical Engineering 84 (2025) 1–10

Contents lists available at ScienceDirect

Chinese Journal of Chemical Engineering

journal homepage: www.elsevier.com/locate/CJChE

Full Length Article

Deep learning approach for morphology classification and particle sizing of industrial methanol-to-olefins (MTO) catalyst

Qingyu Wang [1], Duiping Liu [2], Yong Lu [1], Jibin Zhou [3], Xiangang Ma [3], Mao Ye [3,*]

[1] School of Energy and Environment, Southeast University, Nanjing 210096, China
[2] Yulin Zhongke Innovation Institute for Clean Energy, Clean Energy Innovation Institute of Chinese Academy of Sciences, Yulin 719199, China
[3] Dalian Institute of Chemical Physics, Chinese Academy of Sciences, Dalian 116023, China

ARTICLE INFO

Article history:
Received 17 October 2024
Received in revised form
18 December 2024
Accepted 19 December 2024
Available online 11 March 2025

Keywords:
Catalyst
Particle morphology
Neural networks
Particle size distribution
Irregular particles

ABSTRACT

Accurately acquiring catalyst size and morphology is essential for supporting catalytic reaction process design and optimal control. We report an intelligent catalyst sizing and morphological classification method based on the Mask-RCNN framework. A dataset of 9880 high-resolution images was captured by using a self-made fiber-optic endoscopic system for 13 kinds of silicoaluminophosphate-34 (SAPO-34) catalyst samples with different coke. Then there were approximately 877881 individual particles extracted from this dataset by our AI-based particle recognition algorithm. To clearly describe the morphology of irregular particles, we proposed a hybrid classification criterion that combines five different parameters, which are deformity, circularity, roundness, aspect ratio, and compactness. Therefore, catalyst morphology can be classified into two categories with four types. The first category includes regular types, such as the spherical, ellipsoidal, and rod-shaped types. And all the irregular types fall into the second category. The experimental results showed that a catalyst particle tends to be larger when its coke deposition increased. Whereas particle morphology remained primarily spherical and ellipsoidal, the ratio of each type varied slightly according to its coke. Our findings illustrate that this is a promising approach to be developing intelligent instruments for catalyst particle sizing and classification.

1. Introduction

It is essential and critical to accurately measure catalyst size, morphology, and distribution for supporting catalytic reaction process design and optimal control [1], especially for methanol-to-olefins (MTO) industrial plants that adopt a fluidized bed reactor-regenerator configuration process [2]. Granular catalyst size and morphology determine reaction performance in a reactor, influencing the minimum fluidization velocity [3], solid circulation rate [4], pressure drop [5], and conversion process [6]. In general, it would be great progress to precisely control catalytic reactions if the preferable catalyst could be screened previously according to its size and morphology [7]. Typically, granular materials with a wide size distribution run much more steadily in an ideal fluidized state in a reactor due to their larger particles being circulated by their smaller ones. This phenomenon indicates that bed porosity and expansion coefficient are improved, which promotes a more fluidized uniform state [8]. Furthermore, non-spherical particles typically exhibit lower fluidization quality, smaller minimum fluidization velocity, and fluidization coefficient than spherical ones under the same volumetric equivalent diameter [9]. In addition, some experimental results also indicate that particle morphology greatly influences material mixing within fluidized beds, and spherical particles can reach an ideal mixing performance compared with the others [10]. Yet the mixing quality of non-spherical particles is still less than that of spherical particles can be improved by increasing gas phase velocity. Among spherical, rod-shaped, and disk-shaped particles, the rod-shaped particles have the greatest difficulty being fluidized under the condition of the fastest gas phase velocity. In contrast, spherical particles are fluidized in superior performance with a lower gas phase velocity [11].

This article is part of a special issue entitled: AI for Chemical Engineering published in Chinese Journal of Chemical Engineering.

* Corresponding author.
E-mail address: maoye@dicp.ac.cn (M. Ye).

https://doi.org/10.1016/j.cjche.2024.12.018

As for particle sizing and its morphology measurement, numerous studies have been carried out, and many powerful lab instruments or industry devices have been developed for different application scenarios. Among them, types of screening devices related to sieving techniques are the most widely applied due to their convenience and economic merits. However, there exists an obvious shortage of them since their measured results can only show the graded size information corresponding to the selected sieve apertures [12]. Additionally, several categories of commercial optical or acoustic granular-size instruments exist based on Mie's theory, with application limited to spherical particle scattering assumption [13,14]. Moreover, catalyst morphology can be observed through micro or nano-imaging techniques with different resolution scales. Unfortunately, their measurement accuracy primarily depends on skilled technician [15] and their inefficiency is due to the lack of intelligent recognition algorithms capable of handling image-based particle characterization [16]. In addition, we gradually understand that there is much deviation in which a non-spherical particle with a complex morphology is described by its equivalent diameter. To tackle this fault, various researchers have proposed more morphological parameters such as deformity, circularity, aspect ratio, *etc*. So far, there is still a lack of a common theory to classify particles in an identical criterion.

In this highly digitized world, artificial intelligence techniques have been reshaped with extensive technology integration opportunities, especially for image processing applications. Indeed, it is one of the hot and cutting-edge topics that AI-based image analysis makes granular material size measurement more reliable and efficient [17–20]. Classical deep learning models like U-Net [21] and YOLOv5-Seg [22] have been successfully applied to solve particle image segmentation tasks. The region-based convolutional neural networks (RCNN) have been certified and promise significant advantages in particle image segmentation. This neural network model can offer more precise particle spatial localization and segmentation information under complex environments. An RCNN model was applied to measure bubbles in gas-liquid multiphase flows with 84% prediction accuracy [23]. All these AI achievements will help with catalyst sizing and morphological classification research in an intelligent period.

To address the issues above, we propose an intelligent catalyst sizing and morphological classification method based on the Mask-RCNN framework, which was applied to investigate a dataset of 9880 high-resolution images of 13 kinds of SAPO-34 catalyst with coke from 0% to 9.35% were shot by using a self-made fiber-optic endoscopic. Furthermore, we developed a hybrid classification criterion to tackle the morphological drawback for describing a non-spherical particle by equivalent diameter. This criterion combines five different parameters, which are deformity, circularity, roundness, aspect ratio, and compactness. Finally, we have successfully extracted more than 877881 particles from the 13 catalyst samples image dataset and investigated their sizes and morphological characteristics in detail.

2. Principle of AI-based Particle Size and Morphology Measurement

Fig. 1 illustrates the principle of the AI-based particle size and morphology measurement, which was developed from the Mask-RCNN convolutional neural network model [24]. Its main functions consist of AI-based particle recognition, multi-parameter particle morphology classification, as well as statistical calculations for particle size, morphology, and distribution for each sample. The first function unit of particle recognition includes a fiber-optic endoscopic platform to capture high-resolution particle images. Then an AI-based particle recognition algorithm, a Mask-RCNN neural network, is employed to extract each individual particle on every sample image. After processing the mask images of these individual particles, the data of their size and geometric parameters can be figured out, forming the data set for further statistical analysis. The second is the criteria of a multi-parameter particle morphology classification, which was based on the five conventional parameters such as deformity [25], circularity [26], roundness, aspect ratio, and compactness. By using a bisecting K-means clustering algorithm, the morphology of all sample individual particles can be classified into two categories (regular and irregular) and four subtypes such as spherical, ellipsoidal, rod-shaped, and irregular type by using the process bisecting K-means clustering algorithm [27].

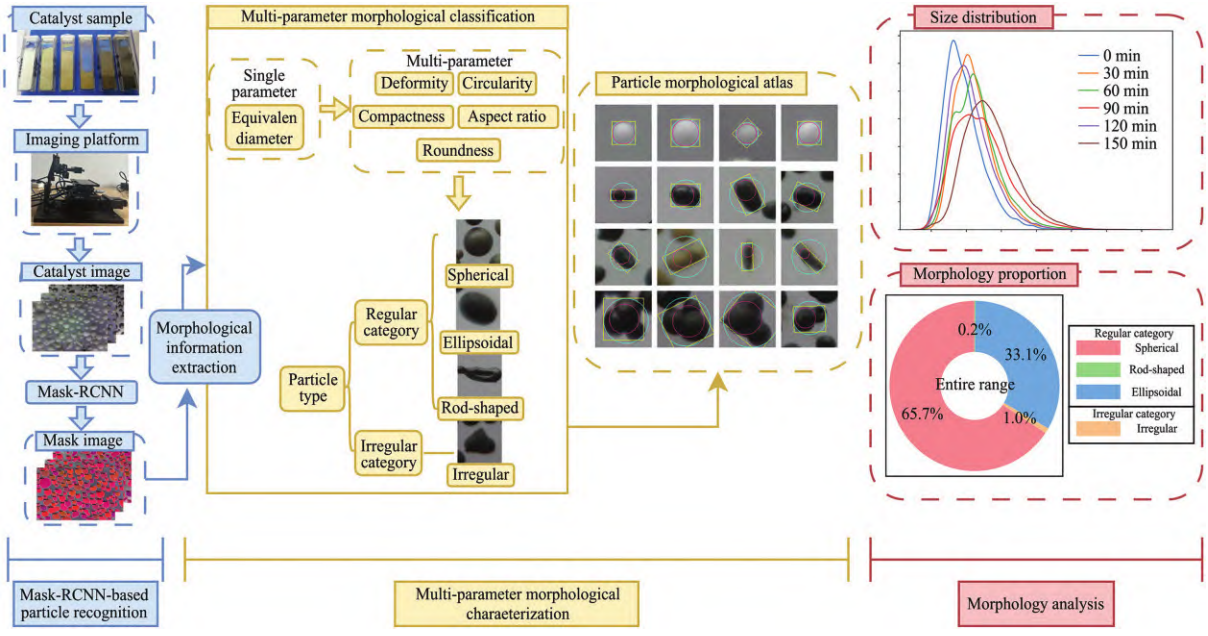

Fig. 1. The framework of the proposed method.

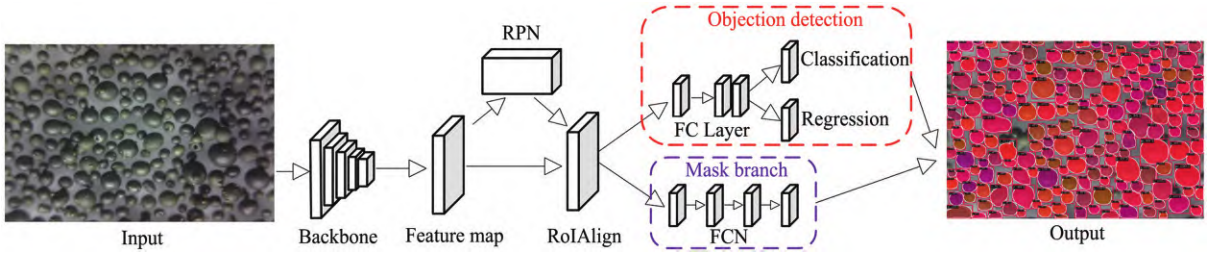

Fig. 2. Network architecture of the Mask-RCNN.

The last is the module for statistically analyzing and illustrating the measured particle data.

3. Deep Learning-based Intelligent Recognition of Catalyst Particles

3.1. Selection of catalyst samples and dataset creation

The MTO process efficiently converts methanol into light olefins, such as ethylene and propylene, which are key raw materials for producing plastics, synthetic rubber, and other chemicals. Due to its exceptional catalytic performance, including high selectivity and conversion rates, the SAPO-34 molecular sieve is widely used as a catalyst in the second generation of the MTO process [28]. We synthesized 13 different SAPO-34 catalyst samples with residence times ranging from 0 to 180 min and coke content varying from 0% to 9.35%.

To achieve an optimal particle size for smooth fluidization, we excluded particles larger than 160 μm and smaller than 10 μm. Particle images were captured using a custom-built fiber-optic endoscopic imaging platform [29], which comprises a particle disperser, a dual-axis high-precision automatic displacement stage, six fiber-optic probes, and a strip light source. Housed in a light-proof box to eliminate interference from ambient light, this device ensures high-quality and consistent imaging conditions.

The image acquisition process for each catalyst sample followed a systematic procedure. First, a disperser was used to evenly spread the catalyst particles onto a glass surface, ensuring minimal particle overlap or adhesion. Next, six probes were employed to capture high-resolution images covering the entire measurement window (90 mm × 100 mm). Each probe captured a target area of approximately 2 mm × 2 mm, with each image having a resolution of 1280 × 960 pixels and containing around 100–150 individual particles. For each sample, approximately 760 images were collected.

We selected 220 images from the collected dataset to create the dataset, which was then split into an 80% training set and a 20% validation set. Particle labeling was performed using the LabelMe program [30], in which particles were annotated as polygons. The JSON files generated by LabelMe were subsequently converted into COCO format, creating annotation files for the particles.

3.2. Mask RCNN neural network

Mask-RCNN (mask region-based convolutional neural network) is a powerful and versatile architecture commonly used for image segmentation tasks. Fig. 2 illustrates the architecture of Mask-RCNN, highlighting its key components. As an instance segmentation network, Mask-RCNN not only detects and classifies particles but also generates precise segmentation masks for individual particles. Furthermore, the integration of ROI Align further improves spatial accuracy, ensuring higher precision in mask generation, which is particularly important for detecting irregular particles.

In the experiment process, all the training and evaluations were conducted on an Xeon E5-2640 CPU and an RTX 3090 GPU. The Mask-RCNN network was trained using ResNet101 as the backbone, replacing the standard convolutional layers. A stochastic gradient descent optimizer with a momentum of 0.9 and a weight decay of 0.0001 was used, and the training process was carried out over 72 epochs. , The mAP metric from the COCOApi, calculated by averaging the average precision (AP) across multiple intersections over union (IoU) thresholds, was used to evaluate the detection performance of the network. In this study, we report the commonly used AP metrics, AP50 and AP75, which correspond to IoU thresholds of 50% and 75%. Test results are shown in Table 1.

The model achieved an overall mAP value of 60.5%, with an AP50 of 78.3% and an AP75 of 73.0%, demonstrating high accuracy in detecting and segmenting particles at both moderate and stricter IoU thresholds. In addition, the total inference time for the 16-image test set was 44.1 s, averaging approximately 2.76 s per image. This demonstrates the model's high computational efficiency, making it suitable for large-scale image segmentation tasks in industrial particle characterization applications. To assess the particle sizing accuracy of the Mask-RCNN method, We measured a batch of standard particles with a known diameter of 250 μm to validate the method against a ground truth. The mean measured diameter was 255.17 μm, with a standard deviation of 0.40 μm, corresponding to a relative error of only 2.07%. These results further confirm the precision and reliability of the Mask-RCNN method for particle sizing, even when validated against particles with exact dimensions.

Visually, the model accurately detects nearly all particles in the images, identifying a total of 185 particles, with 173 successfully recognized, yielding a detection rate of 93.5%. Notably, several particles around the edges of input and output in Fig. 2 were not detected. However, this does not affect the overall analysis, as these particles are excluded due to insufficient morphological information. The Mask-RCNN generated segmentation masks with high precision inside the agglomerates, showing clear and well-defined boundaries between particles without any overlap. Overall, the model demonstrates strong adaptability to particles of varying morphologies and sizes.

4. Multi-parameter Morphological Characterization of Catalysts

4.1. Selection of morphological parameters

Complete characterization of particle morphology is a complex task. Common parameters used in this process include perimeter (P), area (A), equivalent diameter (D), maximum inscribed circle

Table 1
Image segmentation performance.

	mAP/%	AP_{50}/%	AP_{75}/%
Mask-RCNN	60.5	78.3	73.0

diameter (D_i), and minimum circumscribed circle diameter (D_c). However, distinguishing between different particle morphologies often requires a more sophisticated approach, leading to the development of various shape descriptors or form factors, such as aspect ratio, compactness, circularity, deformity, and roundness. Specifically, deformity reflects the degree of deviation from a perfect sphere, circularity describes how closely a particle resembles a circular shape, roundness measures the smoothness of the particle's contour, compactness indicates the density of the particle relative to its area, and aspect ratio characterizes the elongation of the particle along its principal axes. The corresponding calculation formulas are as follows.

(1) Equivalent diameter (D): The diameter of a sphere that has the same projected area as the particle.

$$D = \sqrt{\frac{4A}{\pi}} \tag{1}$$

(2) Circularity (C): Describes the relationship between the ratio of the actual area of a particle to its perimeter and the ideal ratio for a circle.

$$C = \frac{4\pi A}{P^2} \tag{2}$$

(3) Roundness (R_n): A dimensionless indicator that characterizes how close the overall shape of a particle (or its projection) is to a circle.

$$R_n = \frac{4A}{\pi X_{F_{max}}^2} \tag{3}$$

Here, $X_{F_{max}}$ refers to the maximum Feret diameter.

(4) Deformity (D_f): An indicator used to describe how close a particle is to the ideal spherical shape. It is calculated by subtracting 1 from the ratio of the particle's projected area to the area of the maximum inscribed circle.

$$D_f = \frac{A}{A_i} - 1 = \left(\frac{D}{D_i}\right)^2 - 1 \tag{4}$$

(5) Aspect ratio (AR): The ratio of the length to the width of the particle's minimum bounding rectangle.

$$\mathrm{AR} = \frac{\text{Major axis}}{\text{Minor axis}} \tag{5}$$

(6) Compactness (CP): The ratio of the diameter of the largest inscribed circle (D_i) to the diameter of the smallest circumscribed circle (D_c).

$$\mathrm{CP} = \frac{D_c}{D_i} \tag{6}$$

To validate the effectiveness of the parameters mentioned above, we selected a subset of particles from the MTO catalyst samples for detailed analysis. Using the particle segmentation network, we obtained information on 877881 particles in total. From this dataset, we selected 20 representative particles with distinct morphological characteristics (labeled #1 to #20), forming the shape sample set shown in Fig. 3. The morphological parameters of these particles are presented in Table 2. By comparing Fig. 3 with Table 2, the following conclusions can be drawn.

(1) Both roundness and circularity describe how closely a particle resembles a spherical shape. For particles with ideal shapes (*e.g.*, particles #5, #11, #18, and #20), the values for both roundness and circularity are similar and exceed 0.90. However, for rod-shaped or irregular particles (*e.g.*, particles #4, #14, #17, and #18), there is a noticeable difference between these two values. Roundness provides a more accurate representation of the actual particle shape and is more sensitive than circularity in distinguishing the sphericity of particles.
(2) Deformity is defined as the ratio of the particle's projected area to its maximum inscribed circle area minus 1. Thus, the deformity of a spherical particle is 0, and a higher deformity value indicates a greater degree of distortion. In Table 2, particles with deformity values exceeding 1.4 (*e.g.*, #2, #8, and #15) exhibit rod-shaped features, demonstrating that this parameter is highly sensitive in distinguishing between spherical and non-spherical particles.
(3) Compactness describes the tightness of the particle shape. For spherical particles, the compactness ratio is close to 1, while for irregular particles, the ratio deviates from 1. Aspect ratio reflects the ratio of the length to the width of the circumscribing rectangle; an aspect ratio close to 1 suggests a more symmetrical or uniform shape, while deviations from 1 indicate elongation or flattening. Compared to circularity and deformity, aspect ratio and compactness provide a more accurate reflection of non-spherical particle shape. In Table 2, particles #7 and #8 show irregular shapes, with large differences in aspect ratio and compactness, while particles #10 and #19, which are ellipsoidal or rod-shaped, show smaller differences between these values.

Compared to single-parameter methods, this multi-parameter characterization approach offers a more comprehensive representation of the particle shape. It is particularly effective in capturing the detailed features of irregular particles.

4.2. Catalyst shape clustering analysis based on multiple parameters

In this study, the bisecting K-means algorithm, an improved version of the traditional K-means method, was used to classify the particle shapes. It is an improved K-means algorithm, which overcomes some drawbacks of the traditional K-means algorithm and is more robust. The main difference between the bisecting K-means algorithm and the traditional K-means algorithm is that, in the former, only one cluster center needs to be addressed in each iteration according to the sample distribution. Thus, the bisecting K-means algorithm can effectively reduce the chance of falling into local optima and the sensitivity towards noises.

First, we select representative particles from the dataset categorized into four types: spherical, ellipsoidal, rod-shaped, and irregular. Second, the average morphological parameters for each particle type are calculated and used as the initial cluster centers. Finally, the bisecting K-means algorithm is used to cluster the candidate groups based on their morphological parameters.

As seen from Table 3, the dataset of 877881 particles was classified into four distinct shape types: spherical, ellipsoidal, rod-shaped, and irregular shaped. Spherical particles constitute the majority, accounting for 80.95% of the total. These particles exhibit high values for circularity (0.92), roundness (0.95), and compactness (1.07), along with low deformity (0.14) and a nearly uniform

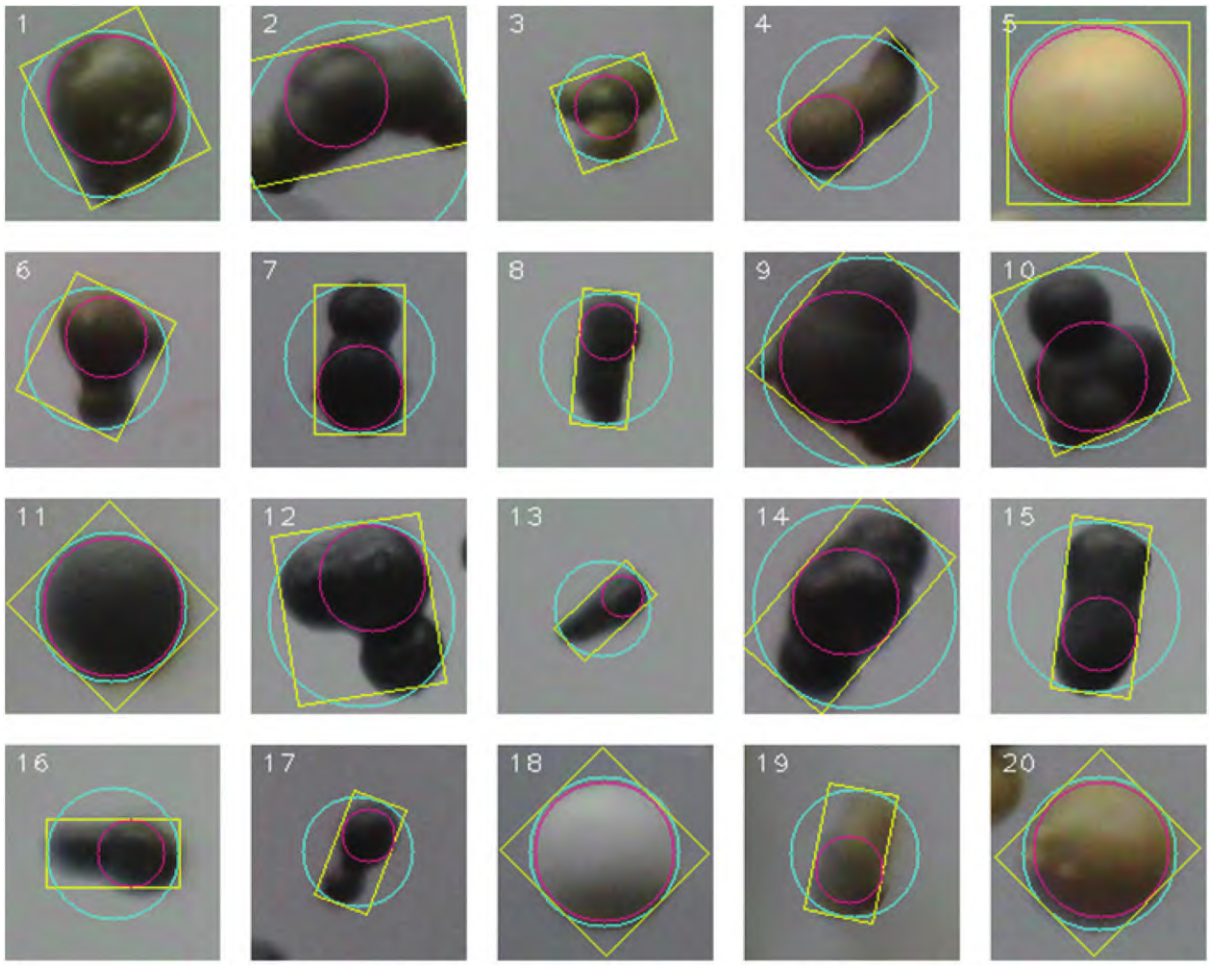

Fig. 3. Catalyst samples in typical morphologies categories.

aspect ratio (1.13), indicating smooth contours and a near-equal balance between length and width.

Ellipsoidal particles represent 16.98% of the dataset. Their characteristic parameters include a circularity of 0.82, roundness of 0.71, deformity of 0.58, an aspect ratio of 1.55, and compactness of 1.47. These particles exhibit relatively smooth contours, but their length is moderately greater than their width, distinguishing them from spherical particles. Rod-shaped particles are a minor

Table 2
Catalyst particle sample morphologies parameters.

Particle ID	Diameter/μm	Circularity	Deformity	Roundness	Compactness	Aspect ratio
1	82.7	0.85	0.28	0.87	1.31	1.20
2	90.6	0.59	1.41	0.43	2.37	1.97
3	51.6	0.75	0.89	0.88	1.65	1.07
4	59.8	0.68	0.89	0.47	2.01	1.99
5	60.7	0.90	0.11	0.99	1.09	1.04
6	63.4	0.68	0.77	0.74	1.67	1.19
7	64.9	0.69	0.80	0.61	1.78	1.66
8	50.0	0.68	1.44	0.44	2.36	2.42
9	97.1	0.73	0.70	0.83	1.59	1.07
10	84.6	0.70	0.84	0.77	1.66	1.19
11	82.9	0.9	0.08	0.97	1.06	1.04
12	83.0	0.68	0.87	0.76	1.73	1.15
13	36.8	0.71	1.13	0.45	2.18	2.18
14	84.3	0.76	0.85	0.54	1.87	1.84
15	68.3	0.73	1.46	0.50	2.23	2.18
16	53.7	0.75	0.8	0.53	1.89	1.95
17	43.1	0.68	0.82	0.48	1.95	1.97
18	82.7	0.91	0.09	0.99	1.07	1.03
19	53.6	0.77	0.87	0.56	1.88	1.85
20	82.7	0.90	0.14	0.97	1.11	1.07

Table 3
Clustering centers and proportions.

Shape		Circularity	Roundness	Deformity	Aspect ratio	Compactness	Proportion/%
Regular	Spherical	0.92	0.95	0.14	1.13	1.07	81.0
	Ellipsoidal	0.82	0.71	0.58	1.54	1.47	17.0
	Rod-shaped	0.73	0.53	1.11	2.02	1.95	0.1
Irregular	Irregular	0.73	0.82	0.81	1.71	1.20	1.9

component, comprising only 0.14% of the total. They are characterized by lower circularity (0.73), roundness (0.53), and high deformity (1.11), with an elongated aspect ratio of 2.02 and compactness of 1.95, highlighting their distinctly elongated shape. Irregular particles make up 1.93% of the dataset. These particles display significant variability in shape, with circularity (0.73), roundness (0.82), deformity (0.81), an aspect ratio of 1.71, and compactness of 1.20. Their irregularity is reflected in the substantial deviations in aspect ratio and compactness, indicating complex shapes that cannot be easily described using regular geometric forms.

For better visualization, the results of multi-parameter morphology classification are shown in Fig. 4. The image contains a total of 84 particles, categorized by shape and color: 63 spherical particles (marked in blue), 19 ellipsoidal particles (marked in purple), 1 rod-shaped particle (marked in green), and 1 irregular particle (marked in red). It is evident that the particle recognition algorithm developed in this study can accurately distinguish the shape of particles.

5. Applications of the AI-based Particle Recognition Method

To acquire more accurate information on catalyst size, morphology, and distribution as well as coke influence, we applied this AI-based particle recognition method to extract about 877881 individual particles from the image dataset of 13 catalyst samples. Then these particles have been quantitively assessed by the above-mentioned five parameters hybrid morphological classification criterion. Their statistical data about size, morphology, and the corresponding distribution are discussed in the following sections.

5.1. Measurement of the fresh SAPO-34 catalyst sample

As for the fresh SAPO-34 catalyst sample, a total of 60840 particles have been recognized by our AI algorithm. Its statistical characteristics related to size and morphology are plotted in Fig. 5, which combines the size cumulative distribution in Fig. 5(a), the size probability density distribution in Fig. 5(b) as well as particle morphological distribution in Fig. 5(c). The key parameters of D_{10} (size cumulative ratio equal to 10%) and D_{90} (size cumulative ratio equal to 90%) were measured as 30.9 μm and 61.6 μm respectively. Consequently, the whole size region can be divided into three sections: smaller size region ($<D_{10}$), middle size region (D_{10}–D_{90}), and larger size region ($>D_{90}$). As depicted in Fig. 5(b), this fresh catalyst sample has an asymmetrical unimodal size distribution with a median diameter of 42.6 μm. In contrast, Fig. 5(c) shows that its morphological characteristics are in the whole size region and the other three sub-size intervals. Most particles in this sample are dominant in the spherical and ellipsoidal types. Their number densities are 65.7% and 33.1% respectively. A small amount of the other two particle types is also found, and the number density data of the rod-shaped and the irregular type are 0.2% and 1%. However, the number density values of the four particle types are different in the three sub-size regions and also different from that in the entire size range. Comparatively, there are two particle types, spherical (95%) and ellipsoidal (5%), in the smaller size region ($<D_{10}$). In the middle size and larger size regions, the ratio of the spherical particles decreases to 63.2% and 56.2%, while that of the ellipsoidal particles increases to 36.1% and 37.6%, respectively. And the other two types, the rod-shaped and the irregular type, also reach (0.2%, 0.5%) and (0.7%, 5.5%) correspondingly.

5.2. Measurement of the other 12 SAPO-34 catalysts samples with coke

In general, a fluidized bed is preferred over a fixed bed reactor as the catalytic reactor for the MTO process [7]. Hence coke influence on catalyst morphology should be further investigated since the MTO reaction over the SAPO-34 catalyst is featured by rapid catalyst deactivation due to the coke deposition. Among our 13 catalyst

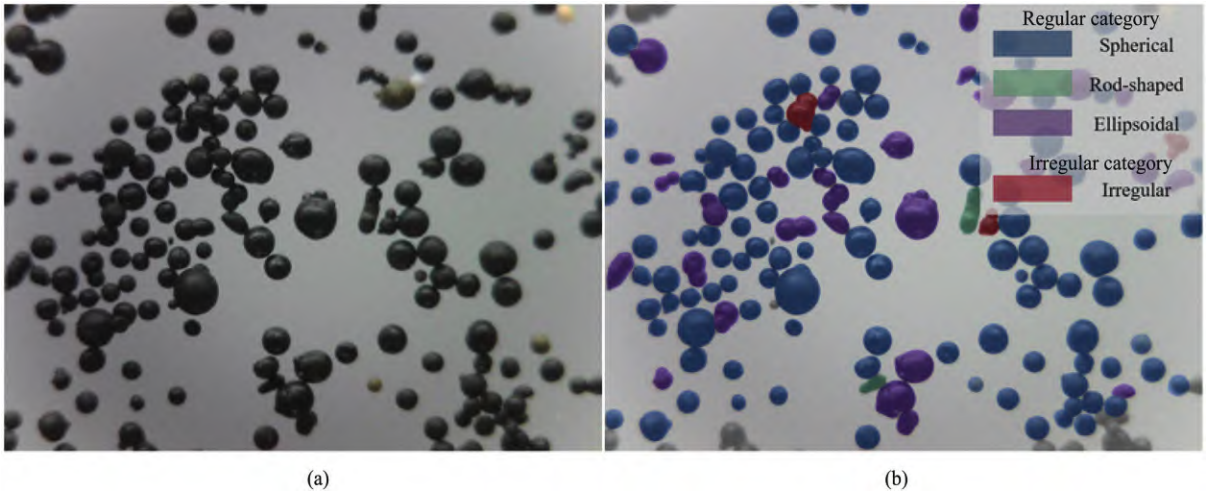

Fig. 4. Particle shape classification.

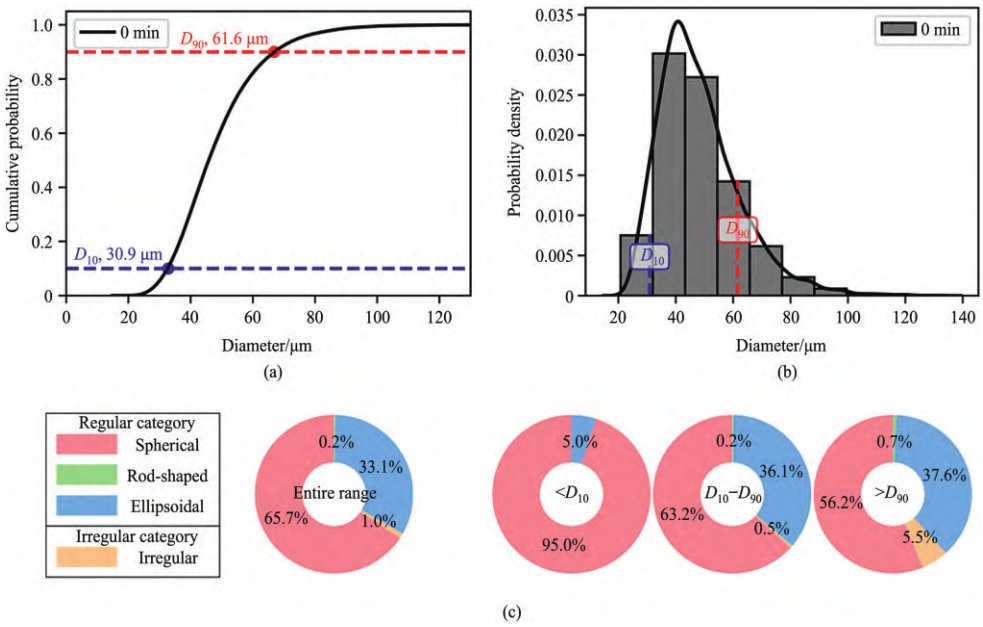

Fig. 5. Size and morphological characteristics of fresh catalyst particles. (a) Cumulative distribution, (b) probability density distribution, (c) morphological distribution.

samples, their coke and the corresponding reaction residence time are listed in the first two columns of Table 4.

It is evident that the coke will deposit much more proportionately with the residence time, especially in the first 150 min of reaction. To evaluate the morphological difference among these 13 catalyst samples, we still discuss them in the three size intervals according to the above-measured D_{10} (30.9 μm) and D_{90} (61.6 μm) in the fresh sample (0 min). The 3rd column in Table 4 lists the data of each total particle number for 13 catalyst samples. Their summation denotes that 877881 particles have been extracted by our AI-based particle recognition method. It can be observed that the number proportion of small particles (<D_{10}) in the fresh sample (0 min) is about 10.0%, whereas that of the other 12 samples deceases rapidly and the minimum value is 0.9% for the two samples with the coke 3.5% and 4.6% respectively. In contrast, the number density of the larger particles (>D_{90}) increases for each 12 samples and the maximum value of the number density is 38.4% for the coke 9.0% sample. Overall, the number of middle-sized particles is relatively stable and fluctuates between 60% and 80%.

Table 4
Size distribution of carbon-deposited catalyst particles.

Residence time/min	Coke/%	Particle count/pcs	Particle number density/%		
			<D_{10}	D_{10}–D_{90}	>D_{90}
0	0	60840	10.0	80.0	10.0
10	1.9	82193	3.0	72.4	24.6
20	2.9	91756	1.9	73.7	24.4
30	3.5	68571	0.9	70.2	28.8
45	4.6	55315	0.9	71.7	27.4
60	5.2	110160	2.7	73.0	24.3
75	6.0	104119	6.6	76.7	16.7
90	6.6	39560	4.0	60.4	35.6
105	7.5	44363	1.2	64.5	34.3
120	8.2	69243	5.0	77.5	17.5
135	8.8	76996	7.7	79.6	12.7
150	9.0	24231	5.9	55.8	38.4
180	9.3	50534	1.5	72.0	26.6

Note: the set value of (D_{10}, D_{90}) is (30.9, 61.6) μm in the fresh SAPO-34 catalyst sample. The total particle count of 13 samples is 877881.

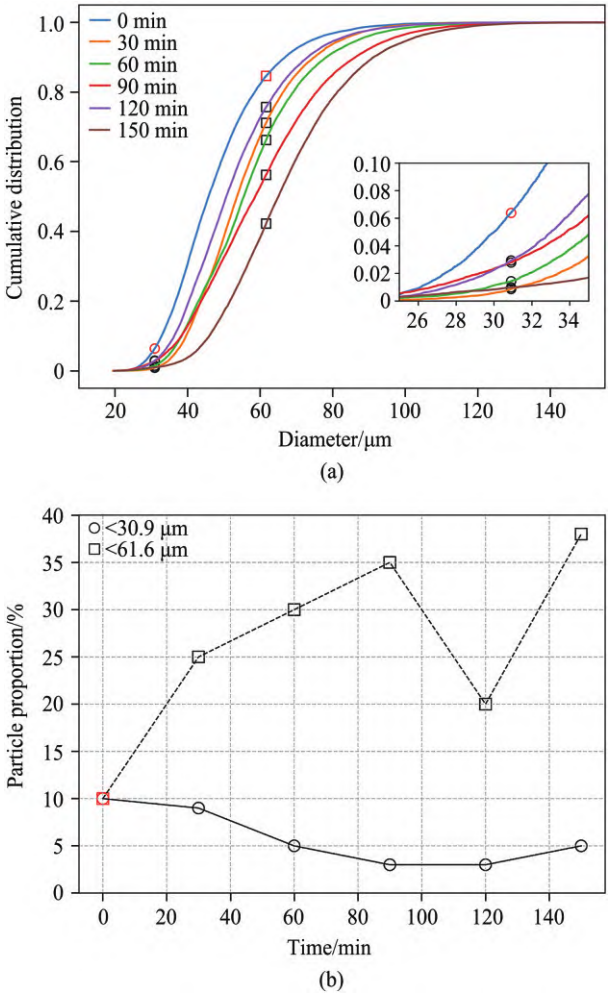

Fig. 6. Size distributions of carbon-deposited catalyst particles: (a) cumulative distribution, (b) proportion of small particles and large particle.

To visualize the influence on catalyst size due to coke deposition, we selected the six samples according to the 30-min time interval between two time-series neighbor samples. As depicted in Fig. 6(a), the cumulative distribution curves of the five selected samples with coke are all positioned to the right of the curve for the fresh sample (0 min). This shift indicates a trend toward larger particle sizes as coke deposition increases. Since the value of (D_{10}, D_{90}) is chosen as the same as that of the fresh catalyst sample, both values of particle density are 10% in the small size region ($<D_{10}$) and the larger size region ($>D_{90}$). Then they are plotted as an overlapped point (depicted in red color) in Fig. 6(b). We choose this set of (D_{10}, D_{90}) as the reference size to count particles less than D_{10} and larger than D_{90} in the other five catalyst samples. The other points in Fig. 6(b) show the variation of particle number density due to coke in the smaller size region ($<D_{10}$) and in the larger size region ($>D_{90}$), respectively.

The proportion of small particles ($<D_{10}$) progressively decreases as residence time increases, dropping from 10.0% at 0 min to 1.9% at 30 min, and reaching a minimum of 0.9% at 45 min. Meanwhile, the proportion of large particles ($>D_{90}$) increases significantly, rising from 10.0% at 0 min to 35.6% at 90 min, and peaking at 38.4% by 150 min.

To quantitatively evaluate particle morphology variations due to coke influence, we defined four kinds of colors such as red, green, blue, and yellow, which correspond to the four particle types which are spherical, ellipsoidal, rod-shaped, and irregular shapes in the particle morphology classification criteria mentioned before. Fig. 7 includes four subfigures that display the variations of

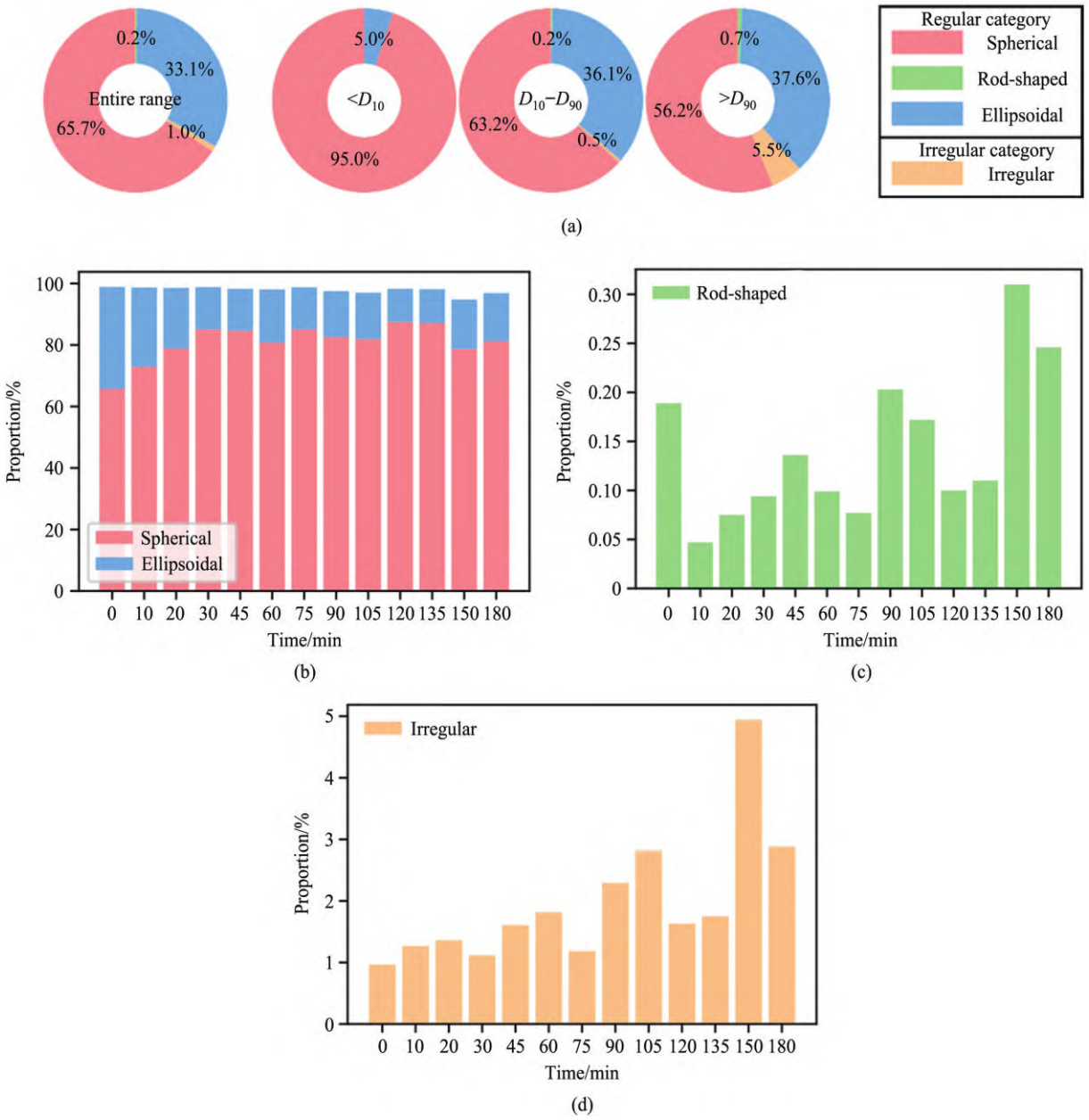

Fig. 7. Particle morphology variations in 13 catalyst samples: (a) morphological distribution, (b) spherical and the ellipsoidal particles, (c) rod-shaped particles, (d) irregular particles.

four particle morphology types in the four size sections of the whole size region, the smaller size region, the middle size region, and the larger size region. According to Fig. 7(a), this pie chart illustrates that the regular shape particles of the spherical and the ellipsoidal occupy over 98% of the total particles of the 13 catalyst samples. As a while, the rod-shaped and the irregular particles account for 0.1% and 1.9% respectively. Additionally, the spherical and the ellipsoidal particles remain dominant and their total ratios are 99%, 98%, and 94% in three sub-size regions. However, the proportions of the other two types (the rod-shaped and the irregular types) vary noticeably. Especially, in the smaller size region, particles with these two types are not found in the total samples. However, in the middle size region and the larger size region, there exist a few rod-shaped particles, although their ratios are only 0.1% and 0.2% respectively. In contrast, the amount of irregular particles varies greatly, and their ratios are 0.8% and 5.3% individually.

To better visualize the morphology differences among the 13 samples, we illustrate the morphological characteristics of our 13 catalyst samples according to the three categories of the group: the spherical and the ellipsoidal, the rod-shaped as well as the irregular type. Fig. 7(a) shows that the group of the spherical and ellipsoidal particles overwhelmingly dominate in each sample. The amount of rod-shaped particles is few and each ratio is less than 1% in total. Meanwhile, each ratio of the irregular type exceeds 1%, although its amount is relatively small and less than 5%.

6. Conclusions

In this work, we presented an intelligent particle recognition method developed from the Mask-RCNN deep learning model combined with classification criteria based on the parameters of deformity, circularity, roundness, aspect ratio, and compactness. The 13 kinds of SAPO-34 catalyst samples were investigated in detail and the main findings of their morphology and particle sizing are summarized as follows.

(1) A dataset including 8777881 individual particles were extracted from 9880 high-resolution SAPO-34 catalyst sample images by our AI-based particle recognition. Their morphology can be classified into two categories with four types such as spherical, ellipsoidal, rod-shaped, and irregular through bisecting K-Means clustering.
(2) As for fresh SAPO-34 catalyst sample, its morphology is dominated to be spherical (65.8%) and ellipsoidal (33.1%). The Rod-shaped (0.2%) and irregular ones (1%) are minor. Its size distribution is relatively uniform, and the key cumulative parameters (D_{10}, D_{90}) are (30.9, 61.6) μm respectively.
(3) Coke has a strong influence on catalyst size, which is indicated by the size distribution curves to be shifted larger with more coke deposition. However, the spherical and ellipsoidal particles are consistently dominated, and the others were less than 5% in total.

Overall, our findings illustrate that this is a promising approach to developing intelligent instruments for catalyst particle sizing and classification. Further studies are undergoing.

CRediT Authorship Contribution Statement

Qingyu Wang: Writing – original draft, Visualization, Software, Methodology, Formal analysis, Data curation, Conceptualization. Duiping Liu: Methodology, Data curation. Yong Lu: Writing – review & editing, Writing – original draft, Supervision, Project administration, Investigation, Funding acquisition, Conceptualization. Jibin Zhou: Methodology, Investigation. XianGang Ma: Supervision. Mao Ye: Supervision.

Declaration of Competing Interest

The authors declare that they have no known competing financial interests or personal relationships that could have appeared to influence the work reported in this paper.

Acknowledgements

This work was supported by the National Natural Science Foundation of China (22308348), the Natural Science Foundation of Liaoning Province of China (2024-MSBA-65), the Qin Chuangyuan Project for Introducing High-Level Innovative and Entrepreneurial Talents (QCYRCXM-2023-024), and the Energy Revolution S&T Program of Yulin Innovation Institute of Clean Energy (E201041206).

References

[1] J.G. Yates, P. Lettieri, Fluidized-Bed Reactors: Processes and Operating Conditions, Springer International Publishing, 2016.
[2] H. Li, Y. Zhao, T. Zhang, Z. Liu, MTO processes development: The key of mesoscale studies, *Adv. Chem. Eng.* 47 (2015) 279–335.
[3] R.T. Feng, J.G. Li, Z.H. Cheng, X. Yang, Y.T. Fang, Influence of particle size distribution on minimum fluidization velocity and bed expansion at elevated pressure, *Powder Technol.* 320 (2017) 27–36.
[4] Y.B. Lin, Q.H. Wang, C. Ye, Y. Zhu, H.J. Fan, Experimental research on the gas-solid flow characteristics in large-scale dual fluidized bed reactor, *Energies* 16 (21) (2023) 7239.
[5] G.M. Karthik, V.V. Buwa, Effect of particle shape on fluid flow and heat transfer for methane steam reforming reactions in a packed bed, *AIChE J.* 63 (1) (2017) 366–377.
[6] P. Rößger, A. Richter, Numerical modeling of a batch fluidized-bed gasifier: Interaction of chemical reaction, particle morphology development and hydrodynamics, *Powder Technol.* 384 (2021) 148–159.
[7] J.T. García-Sánchez, V.G. Baldovino-Medrano, Elements of the manufacture and properties of technical catalysts, *Ind. Eng. Chem. Res.* 62 (20) (2023) 7769–7838.
[8] M. Rasteh, F. Farhadi, G. Ahmadi, Empirical models for minimum fluidization velocity of particles with different size distribution in tapered fluidized beds, *Powder Technol.* 338 (2018) 563–575.
[9] R. Timsina, R.K. Thapa, B.M.E. Moldestad, M.S. Eikeland, Effect of particle size on flow behavior in fluidized beds, *Int. J. EQ* 4 (4) (2019) 287–297.
[10] Y. Shao, B. Jin, W. Zhong, H. Hu, C. Sha, Study on the shape effect of irregular particles mixing behavior in a fluidized bed, *J. Eng. Thermophys.* 35 (3) (2014) 512–516. (in Chinese)
[11] E. Abbaszadeh Molaei, A.B. Yu, Z.Y. Zhou, Particle scale modelling of solid flow characteristics in liquid fluidizations of ellipsoidal particles, *Powder Technol.* 338 (2018) 677–691.
[12] P. Poullet, J.J. Muñoz-Perez, G. Poortvliet, J. Mera, A. Contreras, P. Lopez, Influence of different sieving methods on estimation of sand size parameters, *Water* 11 (5) (2019) 879.
[13] R.L. Xu, Light scattering: A review of particle characterization applications, *Particuology* 18 (2015) 11–21.
[14] P.D. Thorne, I.D. Lichtman, D. Hurther, Acoustic scattering characteristics and inversions for suspended concentration and particle size above mixed sand and mud beds, *Cont. Shelf Res.* 214 (2021) 104320.
[15] M. Naiim, A. Boualem, C. Ferre, M. Jabloun, A. Jalocha, P. Ravier, Multiangle dynamic light scattering for the improvement of multimodal particle size distribution measurements, *Soft Matter* 11 (1) (2015) 28–32.
[16] S. Ramalingam, V. Chandra, Determination of suspended sediments particle size distribution using image capturing method, *Mar. Georesour. Geotechnol.* 36 (8) (2018) 867–874.
[17] A.B. Oktay, A. Gurses, Automatic detection, localization and segmentation of nano-particles with deep learning in microscopy images, *Micron* 120 (2019) 113–119.
[18] P. Rani, S. Kotwal, J. Manhas, V. Sharma, S. Sharma, Machine learning and deep learning based computational approaches in automatic microorganisms image recognition: Methodologies, challenges, and developments, *Arch. Comput. Methods Eng.* 29 (3) (2022) 1801–1837.
[19] M.H. Modarres, R. Aversa, S. Cozzini, R. Ciancio, A. Leto, G.P. Brandino, Neural network for nanoscience scanning electron microscope image recognition, *Sci. Rep.* 7 (1) (2017) 13282.
[20] Y.N. Zhu, Q. Ouyang, Y.D. Mao, A deep convolutional neural network approach to single-particle recognition in cryo-electron microscopy, *BMC Bioinf.* 18 (1) (2017) 348.

[21] A. Colliard-Granero, M. Batool, J. Jankovic, J. Jitsev, M.H. Eikerling, K. Malek, M.J. Eslamibidgoli, Deep learning for the automation of particle analysis in catalyst layers for polymer electrolyte fuel cells, *Nanoscale* 14 (1) (2022) 10–18.
[22] K.P. Treder, C. Huang, C.G. Bell, T.J.A. Slater, M.E. Schuster, D. Özkaya, J.S. Kim, A.I. Kirkland, nNPipe: A neural network pipeline for automated analysis of morphologically diverse catalyst systems, *npj Comput. Mater.* 9 (2023) 18.
[23] R.F.L. Cerqueira, E.E. Paladino, Development of a deep learning-based image processing technique for bubble pattern recognition and shape reconstruction in dense bubbly flows, *Chem. Eng. Sci.* 230 (2021) 116163.
[24] K.M. He, G. Gkioxari, P. Dollár, R. Girshick, Mask R-CNN, 2017 IEEE international conference on computer vision (ICCV), IEEE, Venice, Italy, 2017.
[25] X. Yin, Y. Li, H. Fan, B. Jiang, Characterization of particle morphology of FCC catalyst, *Acta Petrolei Sin. (Petrol. Process. Sect.)* 39 (1) (2023) 109–119. (in Chinese)
[26] G.H. Bagheri, C. Bonadonna, I. Manzella, P. Vonlanthen, On the characterization of size and shape of irregular particles, *Powder Technol.* 270 (2015) 141–153.
[27] A.K. Jain, Data clustering: 50 years beyond K-means, *Pattern Recognit. Lett.* 31 (8) (2010) 651–666.
[28] J.W. Zhong, J.F. Han, Y.X. Wei, P. Tian, X.W. Guo, C.S. Song, Z.M. Liu, Recent advances of the nano-hierarchical SAPO-34 in the methanol-to-olefin (MTO) reaction and other applications, *Catal. Sci. Technol.* 7 (21) (2017) 4905–4923.
[29] Y. Lu, D. Liu, C. Li, J. Zhou, M. Ye, Experimental study on the morphology and coke amount of MTO catalyst using fiber-optic endoscope image method, *CJChE J.* 73 (6) (2022) 2662–2668. (in Chinese)
[30] B.C. Russell, A. Torralba, K.P. Murphy, W.T. Freeman, LabelMe: A database and web-based tool for image annotation, *Int. J. Comput. Vis.* 77 (1) (2008) 157–173.